Geochemical Perspectives Letters

Primordial noble gas isotopes from immoderate crushing of an Icelandic basalt glass

R. Parai

Supplementary Information

The Supplementary Information includes:

- Sample Information
- Gas Extraction and Processing
- Mass Spectrometry Methods
- WUSTL House Gas Standards
- Elemental Ratios
- Supplementary Tables S-1 and S-2
- Supplementary Figures S-1 to S-6
- Supplementary Information References

Sample Information

The MiðfellRP09 sample was collected by RP at 64°10'09.8"N, 21°03'27.5"W. While Harrison *et al.* (1999) report collection from a quarry 1 km east of the lake, the sample analysed in this study (Fig. S-1) was collected by the lake shore and adjacent to a small municipal waste collection area.

Figure S-1 Pillow basalt and MiðfellRP09 glass. **(left)** Vesicular, olivine phenocryst-rich basalt, glass was abundant (1/4" cold chisel for scale). **(right)** Five pieces of glass over 10 g in mass were analysed in a single crusher chamber.

Gas Extraction and Processing

Five pieces of vesicular glass weighing a total of 10.5627 g were cleaned in distilled water and acetone and then dried. The sample was loaded into a stainless steel cup with ultra-high vacuum aluminium foil liner, separated into three layers by tungsten carbide discs. The cup was loaded in a single large-geometry crusher chamber (see schematic of similar, smaller crusher chamber in Parai *et al.*, 2009). Gases were released by step-crushing driven by a hand-pumped hydraulic cylinder while monitoring the pressure of released gas using an MKS capacitance manometer. An automated, compact, low-internal-volume gas extraction and processing line designed and built at WUSTL was used to prepare gases for analysis using the Nu Noblesse HR 5F5M noble gas mass spectrometer. Noble gases were purified by exposing the gas released by step-crushing to hot and cold SAES NP10 getters. A small aliquot (<1 % of total gas) was separated and analysed on a Stanford Research Systems residual gas analyser to estimate expected signals for He and Ar and to determine how to split the He and Ar prior to inlet to the mass spectrometer. Purified gas was exposed to a Janis cryotrap with a charcoal sorbent at 32 K, trapping noble gases heavier than He. Ne, Ar and Xe were sequentially released from the cryotrap and analysed separately.

Mass Spectrometry Methods

Measurements were made using the Nu Noblesse HR 5F5M in the Department of Earth and Planetary Sciences at Washington University in St. Louis. The source trap current and filament voltage were optimised for Xe analysis and kept constant throughout all analyses, meaning that source tuning was suboptimal for He but was sufficient to make useful measurements -- reproducibility of $^{4}He/^{3}He$ in standards with similar amounts of gas as the sample were routinely <1 %. ^{3}He was measured on an electron multiplier fitted with a slit to enable resolution of $^{3}He^{+}$ from HD^{+}.

Ne was measured by multicollection in high mass resolving power mode, with $^{40}Ar^{++}$ resolved from $^{20}Ne^{+}$. CO_2^{+} was monitored during the run by peak jumping, and a correction for CO_2^{++} interference with ^{22}Ne was made using a CO_2^{++}/CO_2^{+} was 0.01878 (following Parai *et al.*, 2009). The CO_2^{++}/CO_2^{+} was determined by repeated calibrations using background CO_2 in the mass spectrometer at different CO_2 pressures, varied by partially closing the valve to the source getter pump. No relationship with total pressure was observed, consistent with prior studies (*e.g.*, Mukhopadhyay *et al.*, 2012). For mega-crush steps, ^{20}Ne was measured on a Faraday; for all other analyses, all Ne isotopes were measured on electron multipliers.

Ar was also measured by multicollection in high mass resolving power mode to enable resolution of hydrocarbon interferences from $^{38}Ar^{+}$. Chlorine backgrounds were monitored during the run by peak jumping. HCl^{+}/Cl^{+} ratios were calibrated in the same manner as CO_2^{++}/CO_2^{+}, and corrections for $H^{35}Cl$ and $H^{37}Cl$ interferences were made using HCl^{+}/Cl^{+} ratios of 0.17 and 0.18, respectively.

Xenon was measured in three steps, with masses 126, 128 and 130 on the axial mass in successive steps. Source tuning optimised sensitivity over mass resolving power as hydrocarbon interferences could be avoided even with low mass resolving power settings.

Instrument sensitivity, mass discrimination, and reproducibility were determined by repeat analyses of an in-house gas standard made by mixing a ^{3}He-doped helium gas standard and dry air collected in Forest Park, St. Louis. Fifty-eight bracketing standards were run with 13 sample crush steps. Typical sensitivities were ~3.5×10^{6} V ^{4}He *per* ccSTP, 1.7×10^{14} cps ^{20}Ne *per* ccSTP, ~1.8×10^{7} V ^{40}Ar *per* ccSTP, and 2.5×10^{15} cps ^{129}Xe *per* ccSTP. The reproducibility of standards of similar size to crush steps was characterised to estimate uncertainties on measured values (Fig. S-2).

Blanks were determined by following the full procedure for a crush without actuating the hydraulic cylinder that would crush the sample. Blanks were <1 % for He, Ne and Ar for all crush steps. For Xe, blanks were <0.4 % for mega-crush steps, and <5 % for all other steps.

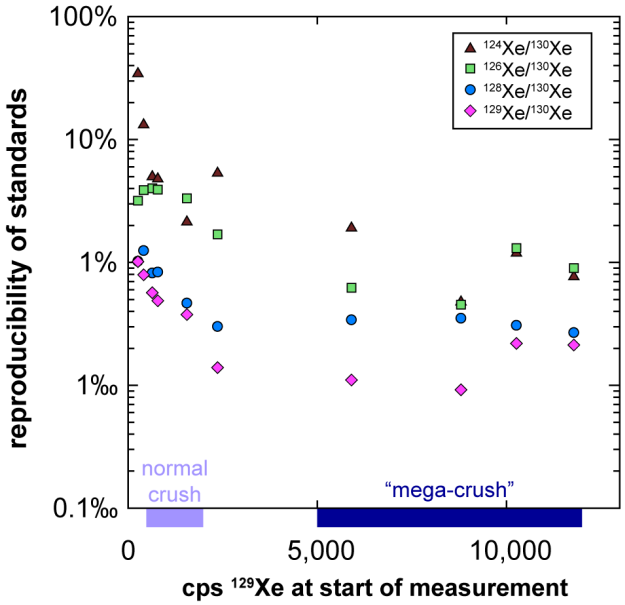

Figure S-2 Reproducibility of standards as a function of signal size. Signal size is shown as counts *per* second of ^{129}Xe at the start of the measurement. Reproducibility is the standard deviation in the isotope ratio measured in a set of standards of a given size divided by the mean isotope ratio for that set. Statistics are shown for ^{124}Xe/^{130}Xe, ^{126}Xe/^{130}Xe, ^{128}Xe/^{130}Xe, and ^{129}Xe/^{130}Xe. The reproducibility of standards at large signal sizes (for mega-crush steps) was 1–2 ‰ in ^{129}Xe/^{130}Xe, and <1 % for the primordial Xe isotope ratios.

WUSTL House Gas Standards

Two house gas standards were mixed in the WUSTL Noble Gas Laboratory. A house helium standard was mixed using a high purity ^{3}He isotope spike purchased from Chemgas (Boulogne-Billancourt, France). A large (8 L) cylinder was prepared along with a helium standard mixing manifold with parts dedicated for the purpose of mixing a helium standard (Swagelok gasket-sealed bellows valves, standard conflat flange fittings, a VAT angle valve, two leak valves and two MKS Baratron capacitance manometers). The cylinder and manifold were rough pumped and all internal volumes were determined using pure nitrogen and MKS Baratron Absolute Pressure Sensors along with a calibrated volume. The system was baked, pumped for several days at ultra-high vacuum, sealed off and transported to a hallway. In this hallway, research-grade ultra-high purity He from Airgas was inlet through one leak valve to fill the 8 L cylinder and portions of the mixing manifold with He (mostly ^{4}He), with the final pressure recorded using a manometer with a 10 torr max range. The ^{3}He spike bottle was attached to the other leak valve and a small volume was filled to a pressure recorded using a manometer with a 0.1 torr max range. Target pressures for both filling steps were calculated to yield a mixture with mantle-like ^{4}He/^{3}He. A valve separating the small volume filled with ^{3}He and the rest of the mixing manifold and cylinder was opened and the system was left to equilibrate for an hour. A VAT all-metal right angle valve was used to seal off the 8 L cylinder, and the helium standard was named LHF, with a calculated ^{4}He/^{3}He of 59,170. The rest of the manifold was pumped out in the hallway using a rough pump borrowed from another lab, and then put into storage.

Two 6 L standard tanks made by Achron Helium Systems (Austin, TX, USA) were prepared: they were pumped out, internal volumes were determined, they were baked and pumped for several days. One 6 L standard tank was attached to a filling manifold along with a ~5 cc volume filled with air collected in Forest Park, St. Louis during exceedingly dry conditions accompanying a polar vortex event in February 2021. The ~1 cc pipette volume of this 6 L tank was filled with a dose of polar vortex air, the outer valve was closed and the inner valve was opened to let the air equilibrate with the cylinder volume.

Both 6 L standard tanks were then attached to a small manifold along with the LHF cylinder. One aliquot from the LHF cylinder was used to fill the pipette volumes (~1 cc) of the two 6 L standard tanks. The outer pipette valves were closed, and the inner pipette valves were opened to let the LHF helium equilibrate with the cylinder volumes. Accordingly, one 6 L standard tank contains an LHF-doped polar vortex air standard named PVA, with ^{4}He/^{3}He of

59,240 and atmospheric Ne, Ar, Kr and Xe isotopic compositions. The other 6 L standard tanks contains LHF. Both standard tanks were installed on the WUSTL gas extraction and purification line.

Elemental Ratios

A manometer directly attached to the crusher chamber was used to monitor pressure during gas release. The manometer records pressure during the crush and after the gas is expanded into a known volume. The drop in pressure is used to determine crusher volume for each crush step. Assuming the dominant species in the released gas is CO_2, moles of CO_2 can be calculated. The estimated $CO_2/^3He$ ratio is 1.3×10^9 (Fig. S-3), in excellent agreement with the value determined for DG2017 (Péron *et al*., 2021), and in broad agreement with measurements of DICE and other mantle samples (Marty and Tolstikhin, 1998; Marty *et al*., 2020).

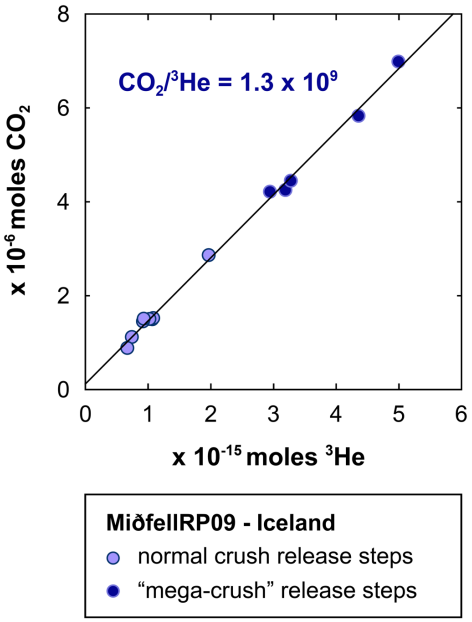

Figure S-3 CO_2 *vs*. ^3He moles released in individual crush steps. CO_2 moles were estimated based on manometer readings and are an upper limit estimate assuming the main volatile species in the released gas was CO_2. There is a good correlation between the manometer pressure and moles of ^3He. This correlation allowed for reliable targeting of “mega-crush” steps with a roughly predictable Xe signal.

The average $^4He/^{40}Ar^*$ ratio is 1.6 (Table S-1), on the low end of the range of estimated mantle production ratio, and the average $^4He/^{21}Ne^*$ is 1.7×10^7, low compared to the mantle production ratio (Yatsevich and Honda, 1997; Graham, 2002). These values are also lower than those measured in the DICE sample (Mukhopadhyay, 2012), indicating that elemental abundance ratios in the MiðfellRP09 sample have been affected by fractionation.

Plotting elemental ratios against isotopic ratios yields arrays that are rotated compared to DICE (Mukhopadhyay, 2012) in a systematic fashion consistent with kinetic fractionation driving preferential loss of He compared to heavier noble gases. He-Ne and He-Ar systematics are illustrated in Figure S-4; element ratio-isotope ratio diagrams involving Xe are highly scattered.

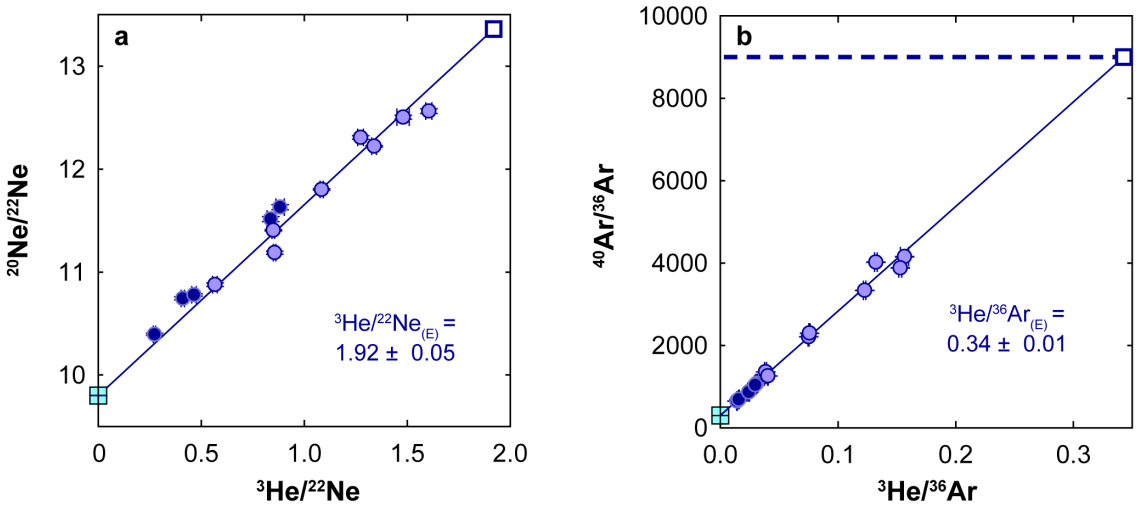

Figure S-4 Elemental ratio *vs*. isotope ratio plots for MiðfellRP09 crush step data. Symbols as in Figure S-3. Good correlations are evident in **(a)** ^{20}Ne/^{22}Ne *vs*. ^{3}He/^{22}Ne and **(b)** ^{40}Ar/^{36}Ar *vs*. ^{3}He/^{36}Ar. Extrapolated mantle source elemental ratios are given for a model mantle with ^{20}Ne/^{22}Ne = 13.36 (solar nebular gas), and ^{40}Ar/^{36}Ar of 9000. The resulting mantle ^{3}He/^{22}Ne and ^{3}He/^{36}Ar are low compared to mantle ratios estimated in studies of the DICE sample (Mukhopadhyay, 2012; ^{3}He/^{22}Ne of ~2.5 at the same ^{20}Ne/^{22}Ne and ~0.75 at the same ^{40}Ar/^{36}Ar as used here). The MiðfellRP09 ^{3}He/^{22}Ne and ^{3}He/^{36}Ar can be used to estimate a mantle ^{22}Ne/^{36}Ar of ~0.18, lower than estimated by Mukhopadhyay (2012), but similar to the value used by Williams and Mukhopadhyay (2019) for Iceland. All of the estimated mantle elemental ratios are depleted in the light element, consistent with kinetic fractionation effects and low ^{4}He/^{40}Ar* and ^{4}He/^{21}Ne* ratios.

Supplementary Tables

Table S-1 He, Ne, Ar, Xe and CO_2 abundances, He, Ne, Ar and Xe isotopic compositions and elemental abundance ratios in step-crush analyses of MiðfellRP09.

Table S-1 (.xlsx) is available for download from the online version of this article at https://doi.org/10.7185/geochemlet.2331.

Table S-2 Mantle source isotope ratios determined using total least squares fits to air-mantle mixing models.

	^{21}Ne/^{22}Ne$_{(E)}$	^{40}Ar/^{36}Ar$_{(E)}$	^{129}Xe/^{130}Xe$_{(E)}$	^{129}Xe/^{132}Xe$_{(E)}$
MiðfellRP09	0.0373	9000	6.85	1.032
±1σ	0.0003	(n/a) See Figure S-5	0.04	+0.003 −0.002

Supplementary Figures

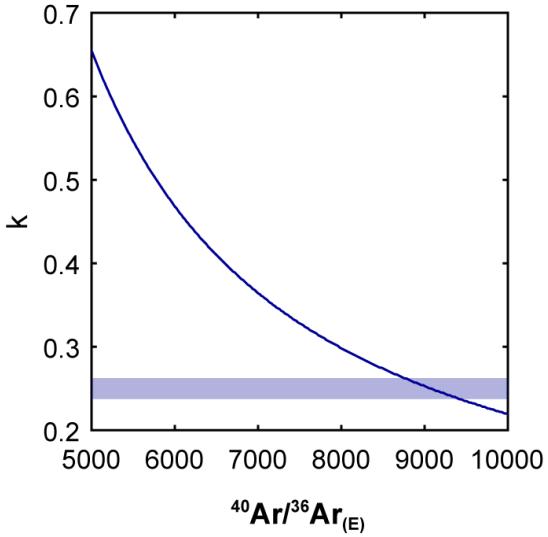

Figure S-5 Best fit mantle $^{40}Ar/^{36}Ar_{(E)}$ as a function of hyperbolic mixing curvature parameter. Total least squares hyperbolic fitting using a mantle $^{20}Ne/^{22}Ne$ of 13.36 did not yield a well-resolved mantle source $^{40}Ar/^{36}Ar_{(E)}$ due to scatter in the data in Ne-Ar space (Fig. 2a). Fits with similar total scores could be achieved with many pairings of mantle $^{40}Ar/^{36}Ar$ and the curvature parameter k (where k values close to 1 approach linear mixing). The curve shows best pairings of these two parameters and illustrates how curvature can be strengthened to compensate for higher $^{40}Ar/^{36}Ar$. Applying a curvature parameter (k = 0.25) consistent with the contrast between $^{36}Ar/^{22}Ne$ in the atmosphere and that estimated for the Iceland mantle source (Williams and Mukhopadhyay, 2019) yields a $^{40}Ar/^{36}Ar_{(E)}$ of ~9000, which is adopted for the Ar-Xe fits shown in Figure 2.

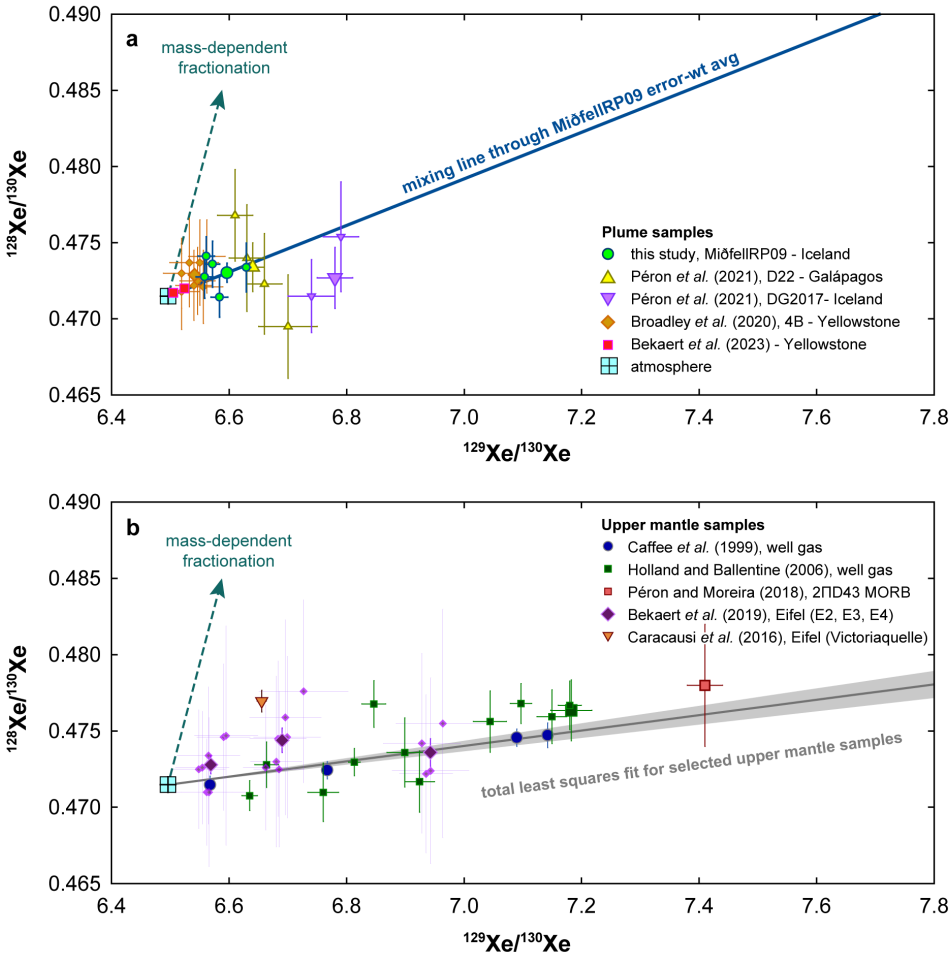

Figure S-6 Individual and average $^{128}Xe/^{130}Xe$ *vs.* $^{129}Xe/^{130}Xe$ data for **(a)** plume and **(b)** upper mantle samples. For samples with differently sized symbols, the small symbols are individual measurements and large symbols are averages, except for the Bravo Dome well gas data from Holland and Ballentine (2006), where the large symbol shows the sample with least atmospheric contamination (BD20-B). The atmospheric composition and a mass-dependent fractionation trend through atmosphere are shown for reference. **(a)** Plume localities include Iceland (this study; Péron *et al.*, 2021), Galápagos (Péron *et al.*, 2021) and Yellowstone (Broadley *et al.*, 2020; Bekaert *et al.*, 2023). With very fine precision enabled by dynamic mass spectrometry, Bekaert *et al.* (2023) showed that volcanic gases are susceptible to mass-dependent fractionation due to diffusive transport within the hydrothermal system. Data from Bekaert *et al.* (2023) was screened using a plot of $^{128}Xe/^{130}Xe$ *vs.* $^{136}Xe/^{130}Xe$, which shows a population of samples dominated by mantle-atmosphere mixing and a population dominated by mass-fractionation. Among the samples dominated by mantle-atmosphere mixing, two with small $\delta^{86}Kr/^{84}Kr$ deviations from atmosphere are shown: Crater Hills 2 and Mud Volcano 1. The Yellowstone volcanic gas 4B average (Broadley *et al.*, 2020) is offset from the other Yellowstone measurements and may reflect a mass-dependent enrichment in light isotopes, but is included in the all-plume total least squares fit shown in Figure 4b. Galápagos data obtained using the screened accumulation technique (Péron *et al.*, 2021) is consistent with the MiðfellRP09 data from this study. One of the two individual measurements for Iceland (Péron *et al.*, 2021) agrees well with the other plume data, but the weighted average for Iceland-DG2017 is offset. **(b)** Upper mantle samples include well gases from Eifel (Caracausi *et al.*, 2016; Bekaert *et al.*, 2019), New Mexico, Colorado and Australia (Caffee *et al.*, 1999; Holland and Ballentine, 2006), and a measurement of the N. Atlantic popping rock 2ΠD43 made using the screened accumulation technique (Péron and Moreira, 2018). Eifel data show indications of mass-dependent fractionation and are excluded from the upper mantle total least squares fit.

Supplementary Information References

Bekaert, D.V., Broadley, M.W., Caracausi, A., Marty, B. (2019) Novel insights into the degassing history of Earth's mantle from high precision noble gas analysis of magmatic gas. *Earth and Planetary Science Letters* 525, 115766. https://doi.org/10.1016/j.epsl.2019.115766

Bekaert, D.V., Barry, P.H., Broadley, M.W., Byrne, D.J., Marty, B., *et al*. (2023) Ultrahigh-precision noble gas isotope analyses reveal pervasive subsurface fractionation in hydrothermal systems. *Science Advances* 9, eadg2566. https://doi.org/10.1126/sciadv.adg2566

Broadley, M.W., Barry, P.H., Bekaert, D.V., Byrne, D.J., Caracausi, A., Ballentine, C.J., Marty, B. (2020) Identification of chondritic krypton and xenon in Yellowstone gases and the timing of terrestrial volatile accretion. *Proceedings of the National Academy of Sciences* 117, 13997–14004. https://doi.org/10.1073/pnas.2003907117

Caffee, M.W., Hudson, G.B., Velsko, C., Huss, G.R., Alexander Jr., E.C., Chivas, A.R. (1999) Primordial Noble Gases from Earth's Mantle: Identification of a Primitive Volatile Component. *Science* 285, 2115–2118. https://doi.org/10.1126/science.285.5436.2115

Caracausi, A., Avice, G., Burnard, P.G., Füri, E., Marty, B. (2016) Chondritic xenon in the Earth's mantle. *Nature* 533, 82–85. https://doi.org/10.1038/nature17434

Graham, D.W. (2002) Noble Gas Isotope Geochemistry of Mid-Ocean Ridge and Ocean Island Basalts: Characterization of Mantle Source Reservoirs. *Reviews in Mineralogy and Geochemistry* 47, 247–317. https://doi.org/10.2138/rmg.2002.47.8

Harrison, D., Burnard, P., Turner, G. (1999) Noble gas behaviour and composition in the mantle: constraints from the Iceland Plume. *Earth and Planetary Science Letters* 171, 199–207. https://doi.org/10.1016/S0012-821X(99)00143-0

Holland, G., Ballentine, C.J. (2006) Seawater subduction controls the heavy noble gas composition of the mantle. *Nature* 441, 186–191. https://doi.org/10.1038/nature04761

Marty, B., Tolstikhin, I.N. (1998) CO_2 fluxes from mid-ocean ridges, arcs and plumes. *Chemical Geology* 145, 233–248. https://doi.org/10.1016/S0009-2541(97)00145-9

Marty, B., Almayrac, M., Barry, P.H., Bekaert, D.V., Broadley, M.W., Byrne, D.J., Ballentine, C.J., Caracausi, A. (2020) An evaluation of the C/N ratio of the mantle from natural CO_2-rich gas analysis: Geochemical and cosmochemical implications. *Earth and Planetary Science Letters* 551, 116574. https://doi.org/10.1016/j.epsl.2020.116574

Mukhopadhyay, S. (2012) Early differentiation and volatile accretion recorded in deep-mantle neon and xenon. *Nature* 486, 101–104. https://doi.org/10.1038/nature11141

Mukhopadhyay, S., Ackert Jr., R.P., Pope, A.E., Pollard, D., DeConto, R.M. (2012) Miocene to recent ice elevation variations from the interior of the West Antarctic ice sheet: Constraints from geologic observations, cosmogenic nuclides and ice sheet modeling. *Earth and Planetary Science Letters* 337–338, 243–251. https://doi.org/10.1016/j.epsl.2012.05.015

Parai, R., Mukhopadhyay, S., Lassiter, J.C. (2009) New constraints on the HIMU mantle from neon and helium isotopic compositions of basalts from the Cook–Austral Islands. *Earth and Planetary Science Letters* 277, 253–261. https://doi.org/10.1016/j.epsl.2008.10.014

Péron, S., Moreira, M. (2018) Onset of volatile recycling into the mantle determined by xenon anomalies. *Geochemical Perspectives Letters* 9, 21–25. https://doi.org/10.7185/geochemlet.1833

Péron, S., Mukhopadhyay, S., Kurz, M.D., Graham, D.W. (2021) Deep-mantle krypton reveals Earth's early accretion of carbonaceous matter. *Nature* 600, 462–467. https://doi.org/10.1038/s41586-021-04092-z

Williams, C.D., Mukhopadhyay, S. (2019) Capture of nebular gases during Earth's accretion is preserved in deep-mantle neon. *Nature* 565, 78–81. https://doi.org/10.1038/s41586-018-0771-1

Yatsevich, I., Honda, M. (1997) Production of nucleogenic neon in the Earth from natural radioactive decay. *Journal of Geophysical Research: Solid Earth* 102, 10291–10298. https://doi.org/10.1029/97JB00395